Int. J. Electrochem. Sci., 16 **(2021)** 150919, doi: 10.20964/2021.01.06

International Journal of
ELECTROCHEMICAL
SCIENCE
www.electrochemsci.org

Effect of Bi_2S_3 on Characteristics of Micro-arc Oxidation Coating formed on TC4 Alloy

Ji Wei Liu[1], *Ping Wang*[1,2*], *Yi Tao Tang*[1], *Dan Xiong*[1], *Xi Yue Sun*[1], *Jie Hu*[1], *Ze Yu Gong*[1], *Biao Yang*[1], *Yun Bai Gong*[1], *Dong Xiang*[1]

[1] School of New Energy and Materials, Southwest Petroleum University, Chengdu, 610500, China
[2] School of Physics, University of Electronic Science and Technology of China, Chengdu, 611731, China
*E-mail: 818wp@163.com

Received: 8 August 2020 / *Accepted:* 19 October 2020 / *Published:* 30 November 2020

Micro-arc oxidation coatings were formed on a TC4 surface with different Bi_2S_3 concentrations (0-0.2 $g{\cdot}L^{-1}$). The influences of Bi_2S_3 on the micro-structure, phase composition, and corrosion resistance of the prepared coatings were investigated by scanning electron microscopy (SEM), X-ray diffraction (XRD), X-ray photoelectron spectroscopy (XPS), and electrochemical workstation. In this research, the MAO voltage first increases and then decreases with an increasing Bi_2S_3 concentrations, which results in similar changes in the thickness and hardness of the coating. XRD and XPS results show that the phase composition of the coating mainly consists of rutile, anatase and Bi_2O_3. The combined result of an increased coating thickness and the presence of anatase promotes coating densification, thereby increasing the corrosion resistance of the coating. Electrochemical polarization curve and impedance results show that the coating has the best corrosion resistance when the Bi_2S_3 concentration is 0.1 $g{\cdot}L^{-1}$. Therefore, the addition of Bi_2S_3 optimizes the microstructure of the MAO coating and enhances its comprehensive properties.

Keywords: Micro-arc oxidation; TC4; Bi_2S_3 particles; Corrosion resistance.

1. INTRODUCTION

In recent years, titanium alloys have been widely used in petroleum, aviation, biology and other fields due to their outstanding physical and chemical properties [1, 2]. TC4 is a titanium alloy composed of an α+β phase. Apart from its high strength and low density, the surface can spontaneously form corrosion resistance films, which have promoted the wide use of TC4 [3-6]. Nonetheless, the film is too thin and is destroyed in harsh environments, which limits the wider application of the alloy [7, 8]. Therefore, extensive research has been conducted on how to modify the surface to obtain a desirable performance that meets various needs [9]. Currently, surface treatment techniques commonly used to improve the performance of titanium alloys include ion implantation [10], sol-gel [11], plasma spraying [12], anodizing [13], chemical vapor deposition [14], micro-arc oxidation (MAO) techniques [15]. Among these techniques, MAO has been well received due to the simplicity of its operation and the environmental friendliness of the electrolyte.

MAO is a new surface treatment developed in recent years on the basis of anodization, which can grow oxidized ceramic-like coatings in situ on the surface of valve metals [16-18]. MAO can prepare a dense coating on the surface of TC4, and the coating has good thermal shock resistance, high hardness and excellent corrosion resistance [19, 20]. Venkateswarlu [21] investigated the MAO treatment of titanium with a mixed electrolyte of phosphate and silicate, and the obtained coating had good corrosion resistance. Li [22] found that when using MAO, the addition of ZrO_2 to a sodium phosphate electrolyte could provide TC4 with good wear resistant coatings. However, few studies have explored the effects of Bi_2S_3 in the MAO coating of TC4. Bi_2S_3 has a low melting point and produces less water pollution. Therefore, this research will fabricate MAO coatings on the surface of TC4 and study the effect of different Bi_2S_3 concentrations.

2. EXPERIMENTAL

2.1. Sample preparation

The conceptual process for preparing MAO coatings is illustrated in Fig. 1. TC4 was used as the substrate material, and its chemical composition is shown in Table 1. Prior to the MAO treatment, all the samples were cut into 15 mm×15 mm×3 mm pieces and mechanically abraded with 800#, 1000#, and 1500# SiC paper. Then the specimens were cleaned with deionized water and degreased with acetone for 10 min. Finally, all specimens were dried in air. The base electrolyte included 6 g/L Na_3PO_4, 4 g/L Na_2SiO_3, 3 mL/L glycol, and 0.5 g/L NaOH, and the concentrations of Bi_2S_3 were 0, 0.05, 0.1, 0.15, and 0.2 $g \cdot L^{-1}$. The corresponding samples were named TC4BS-0, TC4BS-1, TC4BS-2, TC4BS-3 and TC4BS-4, respectively(the abovementioned reagents were supplied by Kelong Chemical Reagent Factory and Cologne Chemicals Limited Company of Chengdu, China).

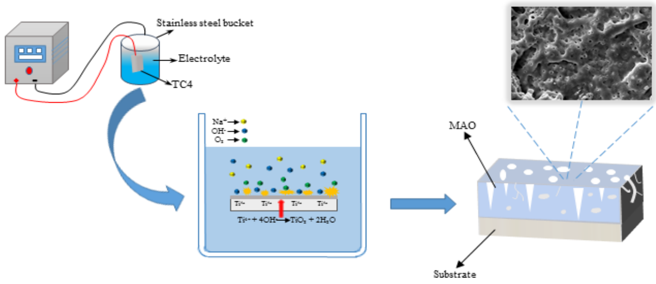

Figure 1. Conceptual process for preparing MAO coatings

During the MAO treatment, an AC power supply of 5 kW was applied. The specimen was used as the anode and a stainless steel bucket was used as the cathode. The duty ratio was 80%, the frequency was 100%, the constant current density was 4.6 $A\cdot dm^{-2}$, and the processing time was 30 min. The temperature of the cell was kept below 30°C. After the MAO treatment, the samples were rinsed with distilled water and dried in air.

Table 1. Composition of the TC4 (wt.%).

Elements	Al	V	Fe	C	O	N	Ti
Content	5.5-6.8	3.5-4.5	≤0.30	≤0.10	≤0.20	≤0.015	Bal.

2.2. Characterization of the MAO coating

The surface morphology and cross-sectional morphologies of the coatings were characterized through scanning electron microscopy (SEM, ZEISS EVO MA15, Germany). The phase composition was identified through X-ray diffraction (XRD, DX-2700B, China), with a scanning step angle of 0.05°, scanning step time of 0.2 s, scattering angle 2θ of 10° to 80° and Cu Kα radiation source generated at 40 kV and 30mA. X-ray photoelectron spectroscopy (XPS) was used to study the surface chemical state and composition. To test the corrosion resistance of the coatings, cyclic polarization curves and electrochemical impedance spectroscopy (EIS) were obtained by an electrochemical workstation (Gamry Reference 3000, America). The coating hardness was evaluated by using a digital micro-hardness tester (HXD-2000TM/LCD, China) at 1 N for 15 s. The coating thickness was measured with a digital thickness gauges (TT230, China). A multifunctional surface performance tester (MFT-4000, China) was used for critical load detection, and a maximum load of 20 N was applied at a loading speed of 10 N/min. Electrochemical tests were conducted in a classical three-electrode system. The specimen served as the worked electrode (1 cm^2 exposed area), platinum electrode as the counter electrode, saturated calomel electrode (SCE) as the reference electrode, and corrosive medium was a 3.5 wt.% NaCl solution. In addition, the thermal shock resistance of the coatings was carried out with a chamber electric furnace (SX-10-12, China). The sample was placed in a furnace heated to 800°C for 10 min, and then chilled in 25°C water for 50 cycles.

3. RESULTS AND DISCUSSION

3.1. Micro-arc oxidation behavior

Fig. 2 is the voltage vs. time of different Bi_2S_3 concentrations. The whole process can be divided into three stages. The first stage (0 ~ 40 s) is named general anodization. During this stage, the voltage increases rapidly, and the coating begins to appear on the surface. The second stage (40 ~ 150 s) is named spark anodization. The increasing rate of voltage decreases compared to the first stage. In addition, the rate of voltage increases for the groups with Bi_2S_3 are higher than the group without. The third stage

(150 s ~) is named MAO. At this stage, the voltage slowly stabilizes and is accompanied by a sharp discharge sound. Clearly, when Bi_2S_3 is greater than 0.1 $g \cdot L^{-1}$, the stable voltage gradually decreases because excessive Bi_2S_3 agglomerates around the coating. This agglomeration prevents the film-forming anions from being adsorbed on the surface of the sample, resulting in a decrease in the coating formation efficiency.

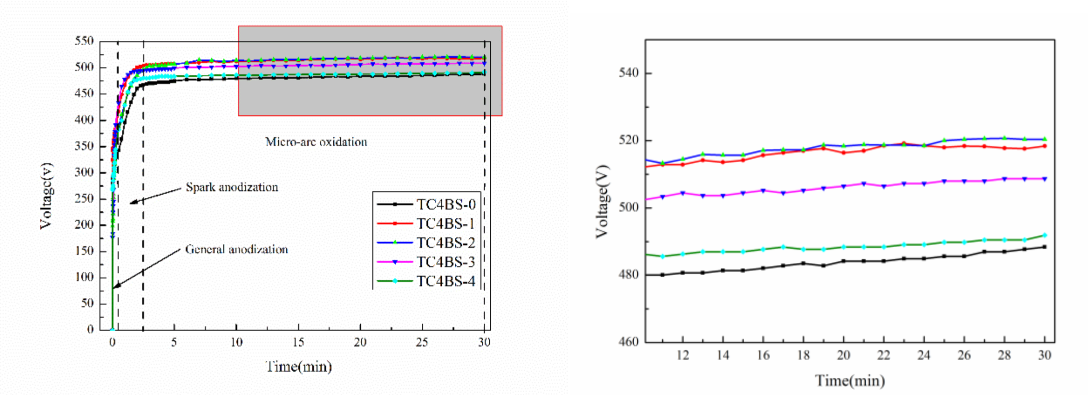

Figure 2. Voltage time curves and local magnification of the MAO coatings prepared with different Bi_2S_3 concentrations

3.2. Phase composition of the coatings

Fig. 3 shows the X-ray diffraction patterns of the MAO coatings at various Bi_2S_3 concentrations and the XPS analysis results of Bi. In Fig. 3(a), the coating without Bi_2S_3 consists mainly of rutile TiO_2, anatase TiO_2 and Ti. The Bi_2O_3 diffraction peak appears when Bi_2S_3 is added. Zhao [23] thought that Bi_2S_3 would be oxidized to Bi_2O_3 when heated to 200-400°C. During the MAO process, the temperature of the discharge channel is as high as 1700°C [24].

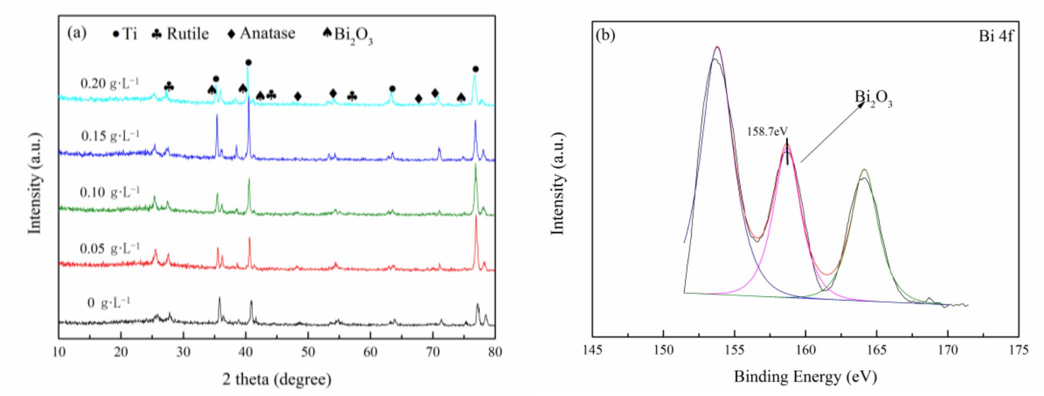

Figure 3. (a) X-ray diffraction patterns of the coatings with different Bi_2S_3 concentrations and (b) the Bi XPS spectra of the MAO coating

Early in the MAO process, molten oxide that forms in the channel encounters the electrolyte. The surface layer rapidly cools thus, TiO_2 mainly consists of an amorphous phase. As the MAO process continues, the amorphous TiO_2 begins to crystallize to form a metastable phase of anatase at the high temperature generated by the frequent micro-arc discharge. As the coating becomes thicker, the temperature inside the coating cannot be cooled quickly, which provides the proper conditions for transitioning from the anatase to the rutile phase; similar findings were found by Hanaor [25]. The Fig. 3(b) shows the XPS analysis result of Bi, and Bi is present in the coating in the form of Bi_2O_3 (Bi 4f : 158.7 eV). The XPS test results correspond to the XRD analysis results.

3.3. Surface micro-structure of the coatings

Fig. 4 shows the surface micro-structure of the MAO coatings with different Bi_2S_3 concentrations. In Fig. 4(a), the surface morphologies are rough and contain many micropores. The main function of these micropores (such as point A) is to act as a channel for the material and energy transfers between TC4 and the electrolyte. With the increase in the Bi_2S_3 concentrations, the pores and diameter first decrease and then increase, which coincides with the change in voltage. As shown in Fig. 5, the coating thickness changes with the voltage. As the coating thickens, the voltage is not enough to penetrate the coating, so the surface micropores change. In TC4BS-2, the number of wavy bumps (as point B) have increased. This result is because the coating is repeatedly broken down, and the reaction product of the discharge channel is under pressure; thus the reaction product is sprayed and deposited around these “crater-like” holes. However, in TC4BS-4, the surface becomes very rough, and even leads to surface ablation (as point C). With this group, a large amount of Bi_2S_3 is suspended in the electrolyte and adheres to the substrate. The discharge localization leads to the accumulation of excessive current, and the surface is ablated by the transient high temperature and pressure.

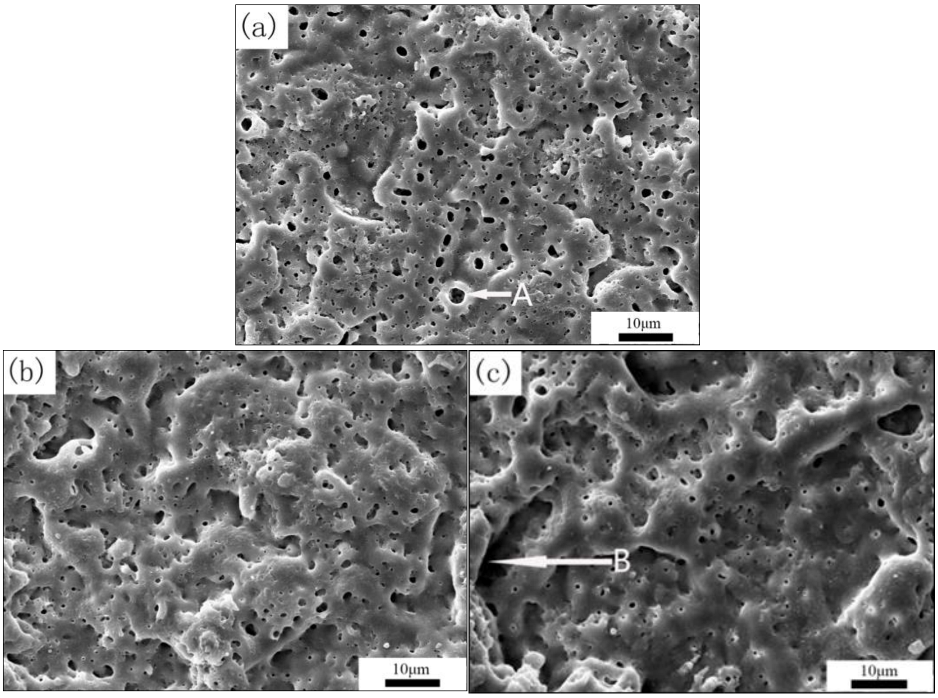

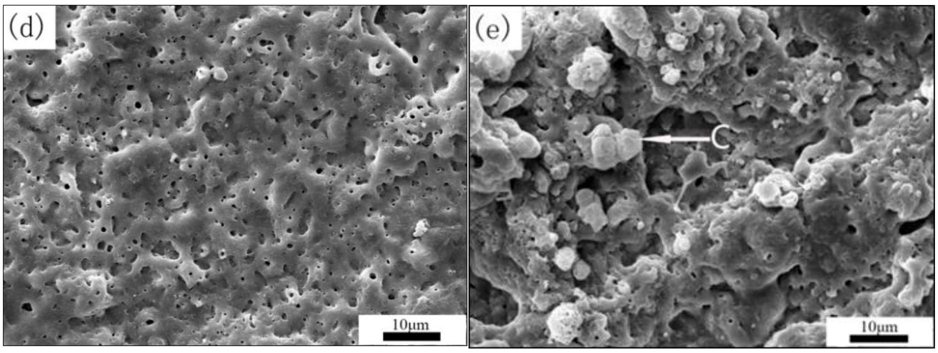

Figure 4. Surface micro-structure of the MAO coatings with different Bi_2S_3 concentrations: (a) TC4BS-0, (b) TC4BS-1, (c) TC4BS-2, (d) TC4BS-3, and (e) TC4BS-4

3.4. Cross-sectional morphologies of the coatings

Fig. 5 shows the cross-sectional morphologies of the MAO coatings with different Bi_2S_3 concentrations. It can be observed that the thickness first increases and then decreases with increasing Bi_2S_3 concentrations. In TC4BS-2, the coating thickness reaches approximately 13 μm, which is consistent with the voltage change in the MAO stage. This phenomenon is related to the discharge intensity and coating deposition rate during the process [26]. The increase in stable voltage intensifies the reaction between the anion in the electrolyte and Ti^{4+}. However, when the Bi_2S_3 concentration is greater than 0.1 $g \cdot L^{-1}$, the discharge is suppressed, which results in a decreased voltage and thin coating thinning.

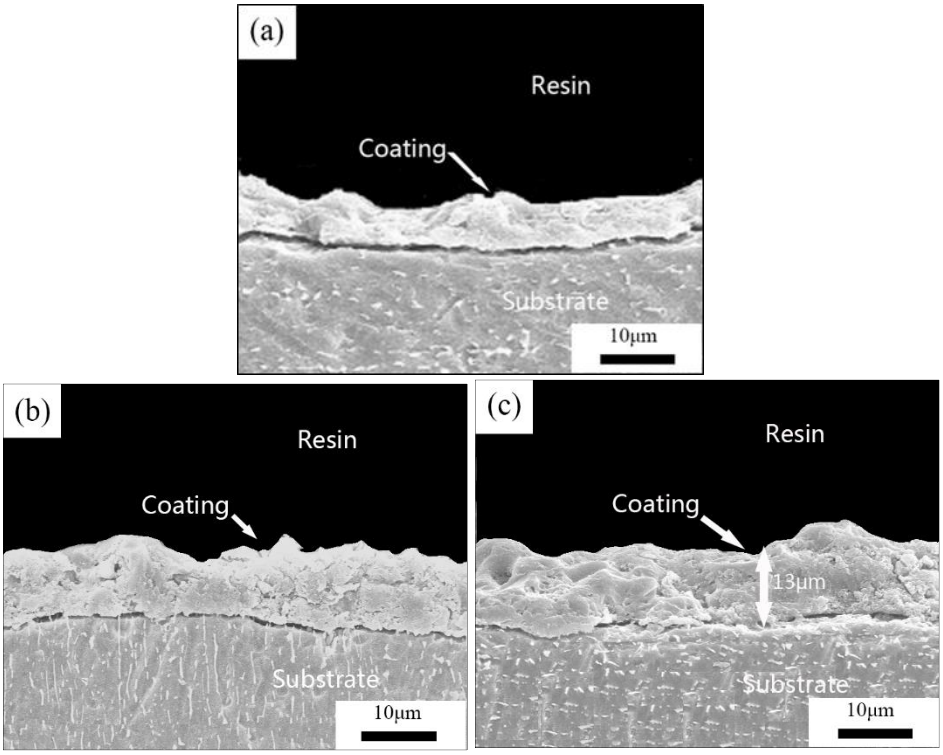

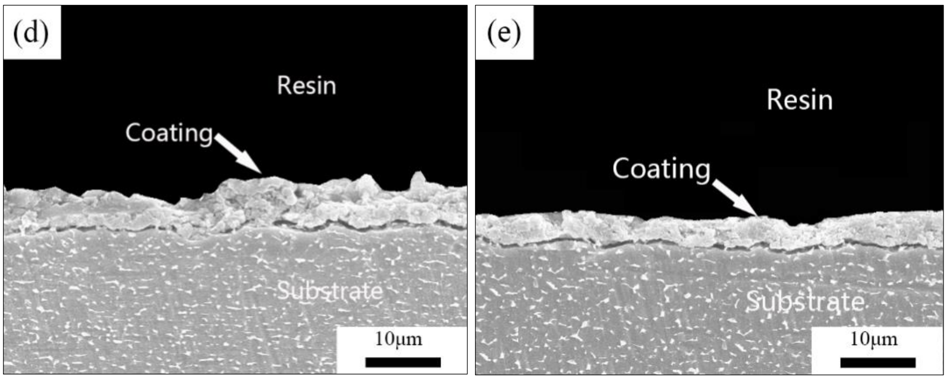

Figure 5. Cross-sectional morphologies of the MAO coatings with different Bi_2S_3 concentrations: (a) TC4BS-0, (b) TC4BS-1, (c) TC4BS-2, (d) TC4BS-3, and (e) TC4BS-4

3.5. Adhesion strength and hardness of the coatings

Fig. 6 shows the adhesive strength and hardness with different Bi_2S_3 concentrations. Adhesion strength is an important mechanical property of rigid films. The in situ growth behaviour provides the coating a high adhesive strength. In this study, the adhesive strength first increases and then decreases with an increasing Bi_2S_3 concentration. The adhesive strength of the coating reaches 16.5 N with TC4BS-2. Similarly, Fig. 5(c) shows that the gap at the junction of the coating base is minimal with TC4BS-2.

The hardness first increases and then decreases with an increasing Bi_2S_3, because the coating thickness and number of micropores change with an increasing Bi_2S_3 concentrations; The temperature cooling inside the coating slows, and the amount of rutile phase increases. Studies have shown that rutile has a higher hardness than anatase [27]. However, in TC4BS-2, the surface ablation of the coating leads to a loose porosity, as shown in Fig. 4(e), thereby decreasing the hardness of the coating.

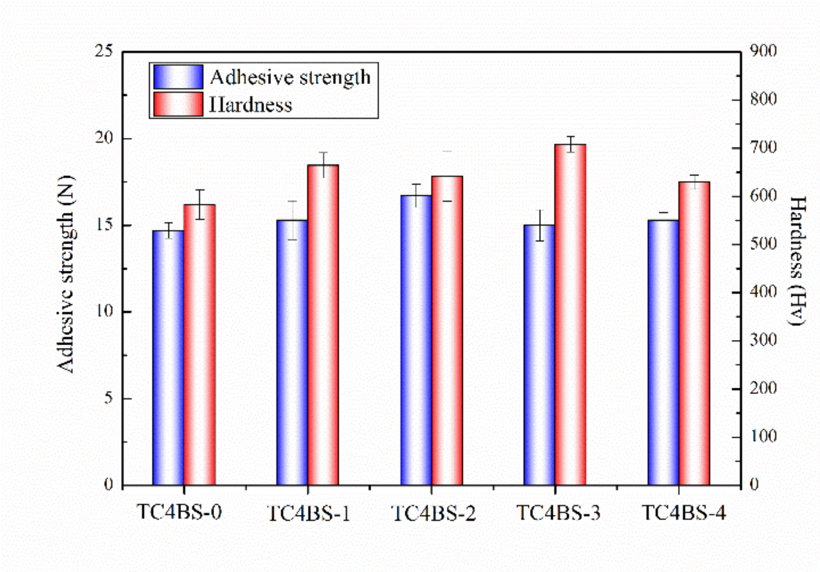

Figure 6. Adhesive strength and hardness of the MAO coatings with different Bi_2S_3 concentrations

3.6. Electrochemical behavior of the coatings

Fig. 7(a) shows the electrochemical polarization curves of the MAO coatings with different concentrations of Bi_2S_3. Using Corr View software to process the experimental data, the self-corrosion potential (E_{corr}), self-corrosion current (i_{corr}) and protection efficiency ($E_{protection}$, %) values are determined by the Stern-Geary equation (Eq (a)); these values are summarized in Table 2.

$$E_{protection} = \frac{i_{corr}^{0} - i_{corr}}{i_{corr}^{0}} \times 100 \qquad \text{(a)}$$

Among the parameters of the polarization curve fitting, i_{corr} is the most significant reference that reflects the corrosion rate of the system [28]. Generally, the corrosion rate varies with the i_{corr} value. It is concluded from Table 2 that the i_{corr} value corresponds to the following order: TC4BS-2 < TC4BS-1 < TC4BS-4 < TC4BS-3 < TC4BS-0 < substrate. In addition, the porosity is a very important factor for the corrosion resistance of the coating. From Fig. 7(b), Cl^- ions reach the substrate through the micropores in the coating; therefore, a decrease in porosity is an important means to improve the corrosion resistance of the coating. Fig. 4(c) shows that when the Bi_2S_3 concentration is 0.1 $g{\cdot}L^{-1}$, the coating is the least porous.

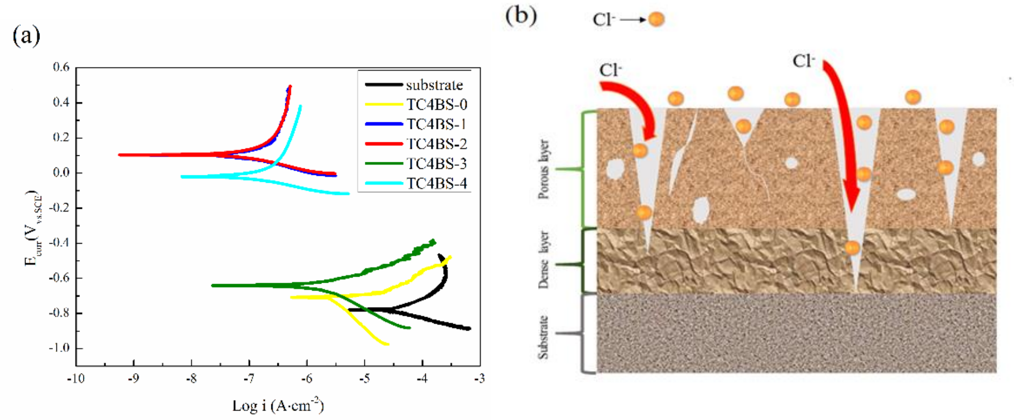

Figure 7. (a) Electrochemical polarization curves of the MAO coatings with different Bi_2S_3 concentrations and (b) the process of corrosion

Table 2. Electrochemical parameters of the polarization curves.

Specimen	E_{corr} ($V{\cdot}SCE^{-1}$)	I_{corr} ($A{\cdot}cm^{-2}$)	$E_{protection}$ (%)
Substrate	-0.78	5.19×10^{-6}	-
TC4BS-0	-0.72	1.92×10^{-6}	63%
TC4BS-1	0.09	2.58×10^{-7}	95%
TC4BS-2	0.11	1.54×10^{-7}	97%
TC4BS-3	-0.66	4.58×10^{-7}	91%
TC4BS-4	-0.50	2.92×10^{-7}	94%

To further research the corrosion resistances of the coatings, the electrochemical impedance curves were also obtained in this experiment [29]. Fig. 8(a) and Fig. 8(b, c) show the Nyquist and Bode plots of the MAO coating with different Bi_2S_3. Fig. 8(a) shows a flat semi-circle, and the arc radius represents the degree of difficulty of the charge transfer. Therefore, the larger the arc radius is, the better the corrosion resistance of the coating [30]. Notably, the TC4BS-1 and TC4BS-2 curves evolve into straight lines, which represent the occurrence of diffusion. The greater the slope of the straight line is, the greater the impedance. Clearly, the arc diameters of the TC4BS-2 coating are the largest.

Fig. 8(b, c) shows the Bode plots fitted by EIS data. Generally, in Bode plots, the porous layer of the coating is located in the high frequency region, and the corresponding, dense layer is represented by the low frequency region. In addition, the dense layer plays the most important role in blocking corrosion ions. Herein, the |Z| of the coating in the low frequency region is arranged as: $|Z|_{TC4BS-2} > |Z|_{TC4BS-1} > |Z|_{TC4BS-3} > |Z|_{TC4BS-4} > |Z|_{TC4BS-0} > |Z|_{substrate}$. Fig. 8 (b) shows the phase angle diagrams. From Fig. 8 (b), the EIS has two time constants. Combined with the Nyquist diagram, the equivalent circuit diagram can be fitted as shown in Fig. 9. In the equivalent circuit, R_s represents the resistance of the corrosion solution, R_p and C_p represent the resistance and capacitance of the porous layer, respectively, and R_d and C_d represent the resistance and capacitance of the dense layer, respectively. R_p and R_d can be used as indicators to measure the performance of coatings on etchant barriers [31], and the results are illustrated in Table 3. The corrosion resistance of the dense layer plays a decisive role in protecting the substrate. All samples are sorted in the following descending order: TC4BS-2 > TC4BS-1 > TC4BS-3 > TC4BS-4 > TC4BS-0. This result is consistent with the above results of the electrochemical polarization curve.

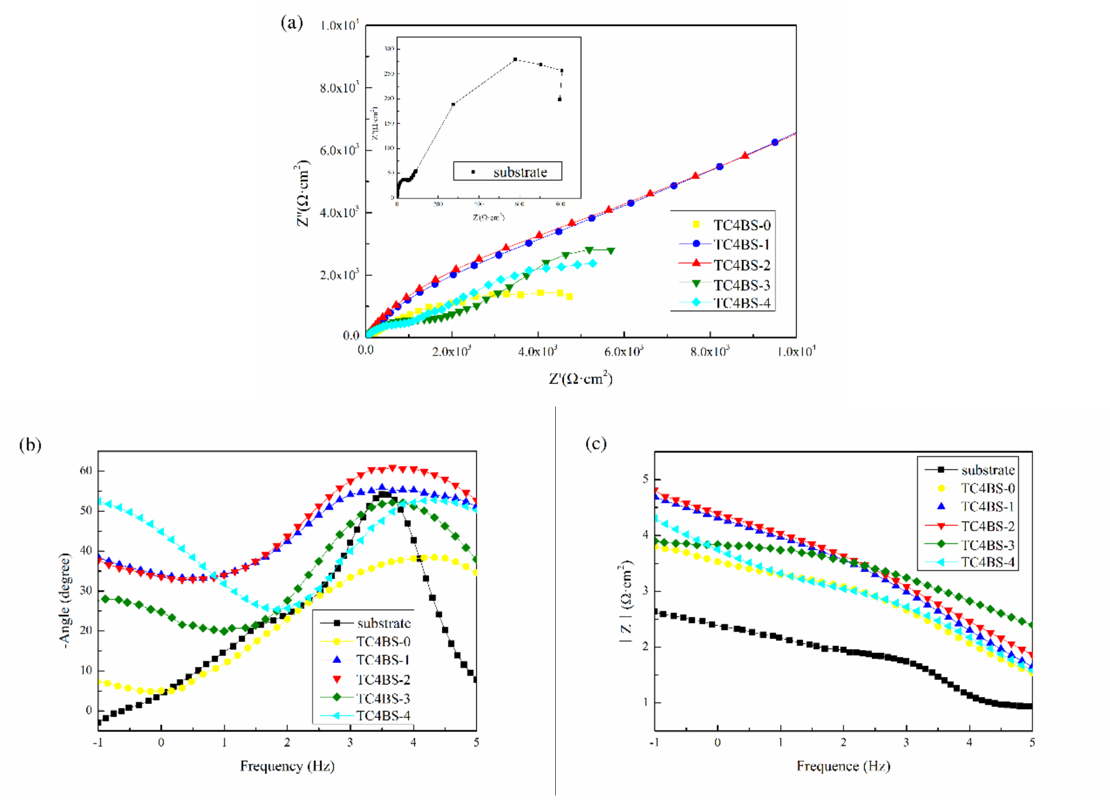

Figure 8. Nyquist plots (a) and Bode plots (b, c) for all samples immersed in a 3.5 wt % NaCl solution

Table 3. Electrochemical impedance parameters.

Specimen	R_s ($\Omega\cdot cm^2$)	C_p		R_p ($\Omega\cdot$cm2)	C_d		R_d ($\Omega\cdot cm^2$)
		Y_0 ($Scm^{-2}S^{-n}$)	n		Y_0 ($Scm^{-2}S^{-n}$)	n	
TC4BS-0	11.04	4.8×10^{-6}	0.8	1588	1.89×10^{-4}	0.8	2.7×10^{4}
TC4BS-1	10.14	1.8×10^{-6}	0.8	6191	2.52×10^{-5}	0.8	6.0×10^{14}
TC4BS-2	9.41	3.3×10^{-6}	0.8	8011	2.16×10^{-5}	0.8	6.9×10^{14}
TC4BS-3	10.46	9.0×10^{-6}	0.73	4068	9.0×10^{-5}	0.75	7.5×10^{4}
TC4BS-4	8.59	4.5×10^{-6}	0.66	1285	6.3×10^{-5}	0.8	6.4×10^{4}

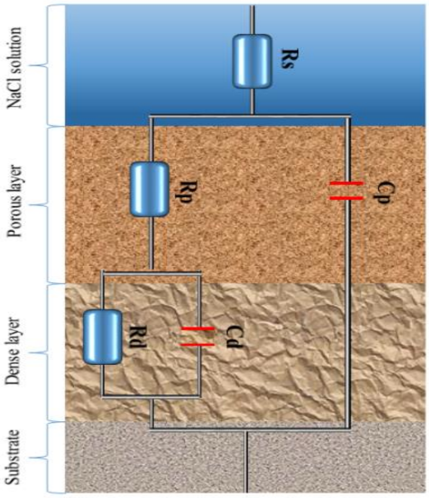

Figure 9. Equivalent circuits and physical model of the MAO coating on TC4

3.7. Thermal shock resistance of the coatings

Fig. 10 shows the TC4BS-0 and TC4BS-4 surface micro-structure before and after a thermal cycling treatment. The group of TC4BS-0 have no obvious cracks appear on the surface after the end of the thermal cycle. However, significant cracking occurs on the surface in the group of TC4BS-4. There are many reasons for the cracking or peeling of the coating, such as the thickness and porosity of the coating. During this thermal shock test, the thermal stress is divided into tensile stress and compressive stress, which occur during heating and cooling, respectively. The stress increases with increasing thermal cycling and eventually leads to the appearance of cracks and the peeling of the coating.

In Fig. 10(a) and (c), the former has significantly more micropores than the latter and can absorb more stress during thermal cycling. Furthermore, it is shown in Fig. 4 that the coating density was TC4BS-4 > TC4BS-0, and the impedance constants of the coating can also be used as evidence. Therefore, the group of TC4BS-4 is more prone to cracking behavior.

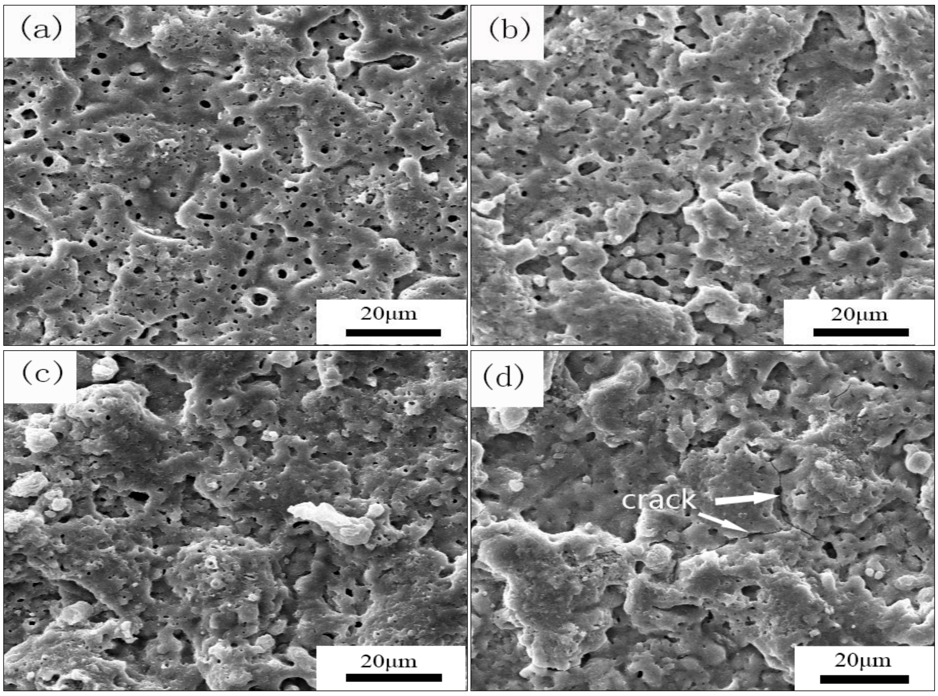

Figure 10. Microscopic topography of the coating before and after thermal the cycling treatment: (a) TC4BS-0 before the thermal shock tests; (b) TC4BS-0 after the thermal shock tests; (c) TC4BS-4 before the thermal shock tests; and (d) TC4BS-4 after the thermal shock tests

4. CONCLUSIONS

1. With the increase in the Bi_2S_3 concentration, the MAO voltage first increases and then decreases, which results in similar changes in the thickness, hardness and adhesive strength of the coating.
2. The main composition of the coating is rutile, anatase and Bi_2O_3. When the Bi_2S_3 concentration was 0.1 $g \cdot L^{-1}$, the micromorphology has the fewest pores, the cross-sectional structure is denser and the thickness reaches the maximum value among the prepared samples. However, surface ablation appears when the Bi_2S_3 concentration is 0.2 $g \cdot L^{-1}$.
3. With the increase in the Bi_2S_3 concentration, the corrosion resistance of the coating first increases and then decreases. When the Bi_2S_3 concentration is 0.1 $g \cdot L^{-1}$, the corrosion resistance of the coating is the best.
4. Thermal cycling causes thermal stress to concentrate between the coating and substrate. Therefore, the addition of Bi_2S_3 will decrease the thermal cracking resistance of the coating.

COMPLIANCE WITH ETHICAL STANDARDS:

FUNDING
China Postdoctoral Science Foundation (2019M663470); The Open Fund of Sichuan Province University Key Laboratory of oil and gas field material (grant number X151519KCL06), Southwest Petroleum University.

CONFLICT OF INTEREST

The authors declare that they have no conflict of interest.

Reference

1. W. P. Wu, J. W. Liu, Y. Zhang and W. Wang, *Surf. Eng.*, 35 (2019) 11.
2. R. Xie, N. Lin, P. Zhou, J. J. Zou, P. J. Han, Z. H. Wang and B. Tang, *Appl. Surf. Sci.*, 436 (2018).
3. Y. Zuo, T. L. Li, P. H. Yu, Z. C. Zhao, X. Y. Chen, Y. Zhang and F. Chen, *Appl. Surf. Sci.*, 480 (2019).
4. P. Wang, T. Wu, Y. T. Xiao, L. Zhang, J. Pu, W. J. Cao and X. M. Zhong, *Vacuum*, 142 (2017).
5. L. L. Ge, N. Tian, Z. X. Lu and C. Y. You, *Appl. Surf. Sci*., 286 (2013).
6. M. V. Diamanti and M. P. Pedeferri, *Corros. Sci*.,49 (2007) 2.
7. C. Wang, J. M. Hao, Y. Z. Xing, C. F. Guo and H. Chen, *Surf. Coat. Tech*., 261 (2015).
8. Y. H. Gu, L. L. Chen, W. Yue, P. Chen, F. Chen and C. Y. Ning, *J. Alloy. Compd*., 664 (2016).
9. S. Jelliti, C. Richard, D. Retraint,T. Roland, M. Chemkhi and C. Demangel, *Surf. Coat. Tech.*, 224 (2013).
10. Y. Yuan, Y. N. Wang, M. Khalid, K. Gao, S. Prucnal, O. D. Gordan, G. Salvan, D. R. T. Zahn, W. Skorupa and S.Q. Zhou, *Ieee. T. Magn*., 50 (2014) 11.
11. M. Zhang, X. Wang, J. Luo and Q. Zhao, *Ieee. T. Electron. Dev*., 58 (2011) 7.
12. X. G. Chen, Y. Yang, D. R. Yan, Y. C. Dong, L. Wang, J. N. He, J. X. Zhang and Z. Z. Li., *J. Mater. Sci*., 46 (2011) 23.
13. T. Lei, C. O. Yang, W. Tang, L. F. Li and L. S. Zhou, *Surf. Coat. Tech.*, 204 (2010) 23.
14. T. S. Katarzyna, K. Koper, A. Mikuła, B. Sahraoui and J. Jaglarz, *Thin. Solld. Films.*, 464 (2018).
15. P. Wang, Z. Y. Gong, J. Hu, J. Pu and W. J. Cao, *Surf. Eng.*, 35 (2019) 7.
16. J. Lee, K. Kuo, K. K. Chiu, J. Kao and B. Lin, *Ieee. T. Plasma. Sci*., 44 (2016) 12.
17. K. J. Wei, L. Chen and Y. Qu, *Surf. Eng*., 35 (2019) 8.
18. J. Xing, Y. J. Chen, C. Y. Yu and M. A. Chen, *Surf. Eng.*, 36 (2020) 2.
19. S. Durdu, Ö. F. Deniz, I. Kutbay and M. Usta, *J. Alloy. Compd.*, 551 (2013).
20. M. Fazel, H. R. Salimijazi, M. A. Golozar and M. R. Garsivaz jazi, *Appl. Surf. Sci*., 324(2015).
21. Venkateswarlu K, Rameshbabu N, Sreekanth D, Sandhyarani M, Bose AC, Muthupandi V and Subramanian S, *Electrochim. Acta.*, 105 (2013).
22. H. Li, Y. Z. Sun and J. Zhang, *Appl. Surf. Sci*., 342 (2015).
23. Y. Zhao , D. L. Gao , J. F. Ni, L. J. Gao, J. Yang and Y. Li, *Nano. Res*., 7 (2014) 5.
24. P. Wang, X. Y. Guo, X. L. Mao, *Rare. Metal. Mat. Eng.*, 43 (2014) 7.
25. Hanaor, D.A.H. and Sorrell, C.C., *J. Mater. Sci*., 46 (2011).
26. P. Wang, X. W. Wei, W. J. Cao, Y. T Tang, Y. Wang, Z. Y. Gong, J. Hu, J. Pu and X. T Zu, *Int. J. Electrochem. Sci.*, 14 (2019) 9.
27. Marques IDSV, Alfaro MF, Cruz NCD, Mesquita MF, Takoudis C, Sukotjo C, Mathew MT and Barao VAR, *J. Mech. Behav. Biomed.*, 60 (2016).
28. Z. Shi, M. Liu and A. Atrens, *Corros. Sci*., 52 (2010) 2.
29. X. Q. Zhan, W. Shang, Y. Q. Wen, Y. Q. Li and M.M. Ma, *J. Alloy. Compd.*, 774 (2019).
30. J. Liang, Z. X. Li, W. B. Yang, F. Zhou, Q. L. YU, Y. Wu and D. A. Wang, *Acs. Photonics.*, 35 (2019) 5.
31. H. P. Duan, K.Q. Du, C. W. Yan and F. H. Wang, *Electrochim. Act*a., 51 (2006) 14.